iScience

CellPress
OPEN ACCESS

Article

Mechanistic insight into deep holes from interband transitions in Palladium nanoparticle photocatalysts

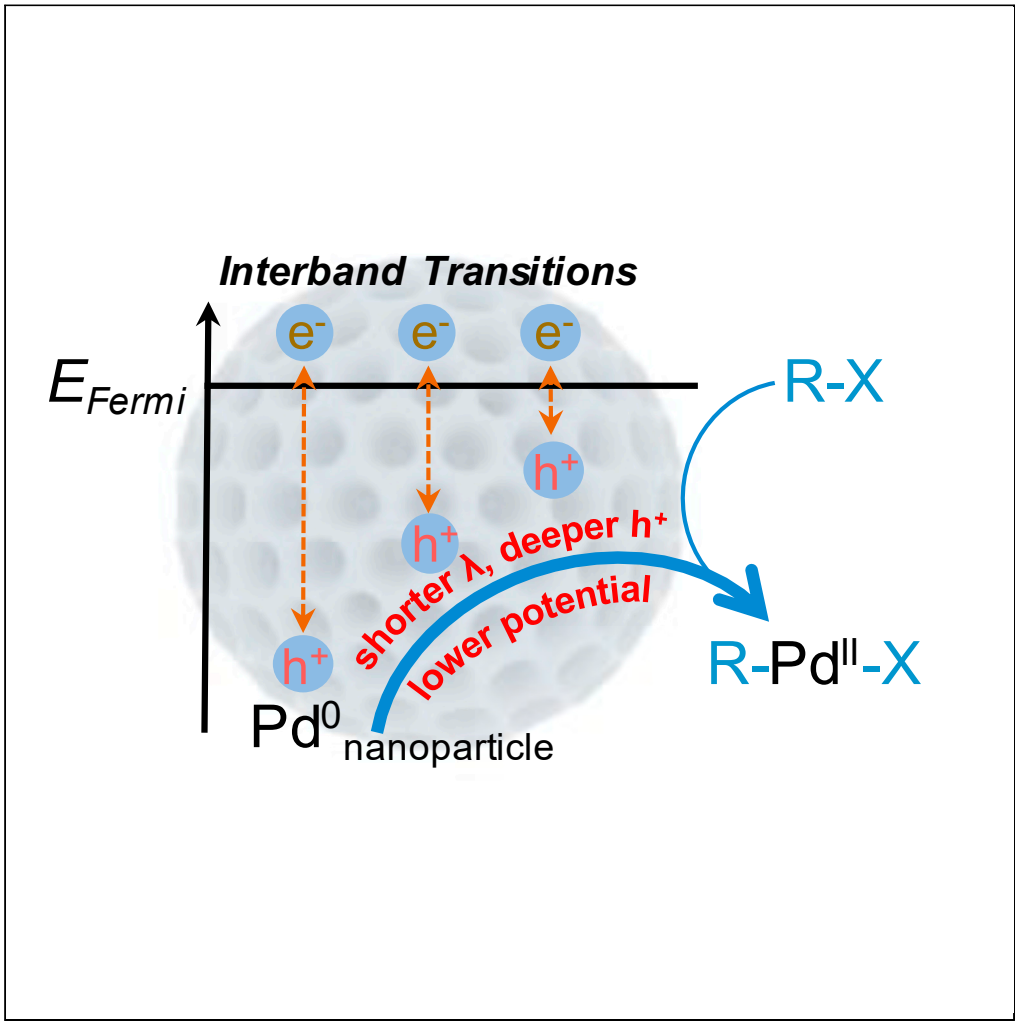

Pin Lyu, Randy Espinoza, Md. Imran Khan, William C. Spaller, Sayantani Ghosh, Son C. Nguyen

son@ucmerced.edu

Highlights

Comparison of quantum yield across different wavelengths

Interband transitions from shorter wavelength excitation offering deeper holes

Deeper holes with stronger oxidizing power for higher quantum yield

Lyu et al., iScience 25, 103737
February 18, 2022
https://doi.org/10.1016/j.isci.2022.103737

iScience

CellPress
OPEN ACCESS

Article

Mechanistic insight into deep holes from interband transitions in Palladium nanoparticle photocatalysts

Pin Lyu,[1] Randy Espinoza,[1] Md. Imran Khan,[2] William C. Spaller,[1] Sayantani Ghosh,[2] and Son C. Nguyen[1,3,*]

SUMMARY

Utilizing hot electrons generated from localized surface plasmon resonance is of widespread interest in the photocatalysis of metallic nanoparticles. However, hot holes, especially generated from interband transitions, have not been fully explored for photocatalysis yet. In this study, a photocatalyzed Suzuki-Miyaura reaction using mesoporous Pd nanoparticle photocatalyst served as a model to study the role of hot holes. Quantum yields of the photocatalysts increase under shorter wavelength excitations and correlate to "deeper" energy of the holes from the Fermi level. This work suggests that deeper holes in the *d*-band catalyze the oxidative addition of aryl halide R-X onto Pd^0 at the nanoparticles' surface to form R-Pd^{II}-X complex, thus accelerating the rate-determining step of the catalytic cycle. The hot electrons do not play a decisive role. In the future, catalytic mechanisms induced by deep holes should deserve as much attention as the well-known hot electron transfer mechanism.

INTRODUCTION

Metallic nanoparticles have gained a growing interest for applications in photocatalysis (Al-Zubeidi et al., 2019; Aslam et al., 2018; Chang et al., 2019; Christopher and Moskovits, 2017; DuChene et al., 2018; Gellé et al., 2020; Huang et al., 2018; Kazuma and Kim, 2019; Kim et al., 2016, 2018; Mao et al., 2019; Seemala et al., 2019; Yu et al., 2019; Zhang et al., 2018, 2019; Zhao et al., 2017; Zhou et al., 2018). The strong light absorption, high surface-area-to-volume ratio, and robust nature of these nanoparticles make them great potential candidates for exploring better photocatalytic activities and high recyclability. Historically, photocatalysis induced by localized surface plasmon resonance (plasmon resonance for short) of these particles has been studied widely for more than a decade (Brus, 2008; Gellé et al., 2020; Hou and Cronin, 2013; Linic et al., 2011; Xin et al., 2018; Yu et al., 2019), but photocatalysis originating from interband excitations is still underexplored (Hou et al., 2011; Huang et al., 2018; Kim et al., 2016; Liu et al., 2014; Zhao et al., 2017). In short, the plasmon resonance can be described by a classical picture as a collective oscillation of the nanoparticles' electrons in response to electric field of exciting photons or a quantum mechanical picture as electron transitions from some *sp*-band states to other *sp*-band states (*i.e.*, intraband transitions), whereas the interband transitions are given to electron transitions from the respective *d* to *sp* bands. Because of these origins, the plasmon resonance of metal nanoparticles offers strong optical absorption and tunable spectral shift depending on the particle morphology, but the interband transitions always provide a significant absorption within a defined spectral region. The optical excitations in these two regimes are expected to exhibit different catalytic outcomes because the generated hot carriers have different energy states, population, and dynamics for each regime (Bernardi et al., 2015; Khurgin, 2020; Sundararaman et al., 2014). With the generation of hot electrons above the Fermi level (E_F) and hot holes near E_F by the plasmon resonance, the extraction of the hot electrons is more favorable than that of the hot holes, and electron transfer from the nanoparticle photocatalysts to reactants (reductive pathway) is generally preferred. This catalytic mechanism has been demonstrated in many reductive reactions, such as reduction of CO_2 or nitro compounds (Gellé et al., 2020; Zhang et al., 2018). Recently, the hot holes could also be utilized for some oxidative reactions, such as alcohol oxidation (Boltersdorf et al., 2018; Kontoleta et al., 2020; Zhang et al., 2020; Zhu et al., 2009). On the other hand, interband transitions, generating "deeper" holes below E_F and electrons near E_F, are more suitable for the oxidative pathway where the nanoparticle photocatalysts are better used for hole-mediated oxidation reactions. This suggested mechanism will provide a new perspective in understanding photocatalysis of metal nanoparticles and designing better photocatalyzed reactions.

[1]Department of Chemistry and Biochemistry, University of California Merced, 5200 North Lake Road, Merced, CA 95343, USA

[2]Department of Physics, University of California Merced, 5200 North Lake Road, Merced, CA 95343, USA

[3]Lead contact

*Correspondence: son@ucmerced.edu

https://doi.org/10.1016/j.isci.2022.103737

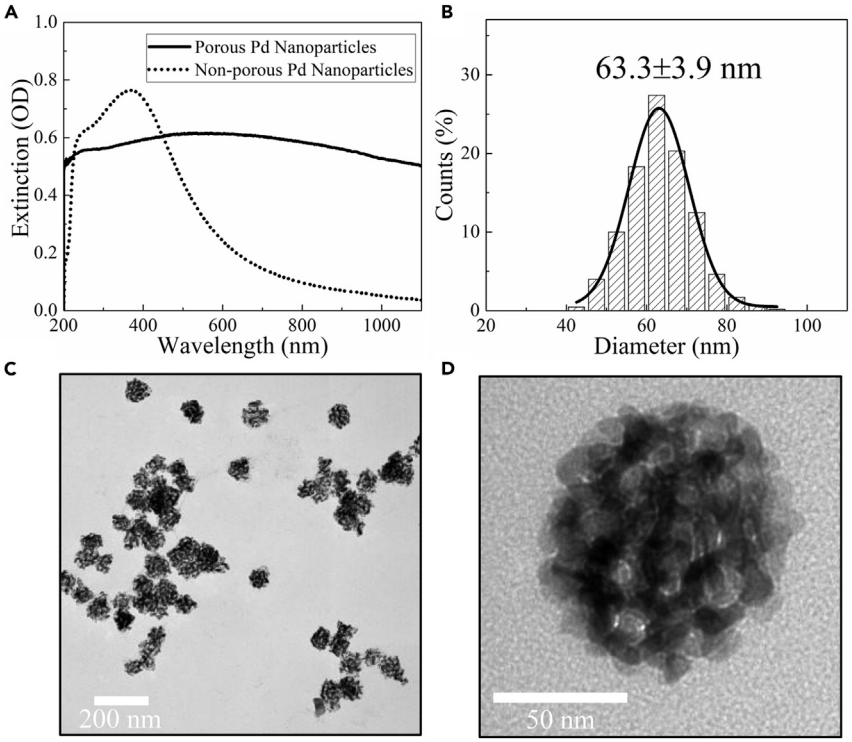

Figure 1. Optical and morphological characterization of mesoporous Pd nanoparticles

(A) UV-Vis spectra of colloidal mesoporous Pd nanoparticles (solid line) in water and nonporous 50 nm Pd nanoparticles solution (dotted line) for comparison.

(B) Size distribution based on analyzing 500 nanoparticles from the SEM image in Figure S3A.

(C and D) Representative TEM images of mesoporous Pd nanoparticles.

To shed light on the catalytic mechanisms in previous experiments, many research groups have compared the catalytic efficiencies under these two excitations, but it has been difficult to disentangle the origin of the observed efficiencies because of the strong spectral overlap of these two excitations (Christopher et al., 2011; Mukherjee et al., 2013; Sakamoto et al., 2015; Yu et al., 2019; Zhao et al., 2017). For example, the plasmon resonance of spherical gold nanoparticle catalysts in the region around 480 to 650 nm is spectrally overlapped with the intrinsic *d*-to-*sp* interband transitions. These interband transitions have a strong absorption in the ultraviolet region and extend to the visible region with an absorption tailed up to about 600 nm (Guerrisi et al., 1975). Thus it is desirable to tune the plasmon resonance absorption away from the interband absorption to resolve the catalytic mechanism. This approach is demonstrated in this paper by using mesoporous structure.

In this study, mesoporous Pd nanoparticles were employed because of their spectral shift of plasmon resonance from visible to near-infrared regions and the dominant contribution of interband transitions in the optical region that we surveyed (*i.e.*, 400-600 nm). Usually, the nonporous Pd nanoparticles have a plasmon resonance associated with a very broad spectral feature in the ultraviolet-visible region, and this plasmonic peak appears on top of the entire spectral region of the interband transitions (Figure 1A).(Langhammer et al., 2006; Niu et al., 2008) In contrast, the porous version shows a featureless absorption with no peak of plasmon resonance in the 400-600 nm region (Figure 1A), therefore the observed photocatalytic activities could be attributed mainly to interband transitions. Another advantage of the mesoporous structure is the shorter travel distance for hot carriers diffusing to particles' surface, thus the efficiency of harvesting them is expected to be improved (Mao et al., 2019).

The Suzuki-Miyaura reaction between bromobenzene and phenylboronic acid in water was used as a prototype reaction to evaluate the catalytic activities induced by interband transitions of porous Pd nanoparticles. Generally, the rate-determining step of this reaction is the oxidative addition of the aryl halide, which was proposed to be accelerated by hot electrons generated from the photocatalysts (Gellé et al., 2020;

Molnár, 2011; Xiao et al., 2014). The performance of these photocatalysts was evaluated by their quantum yields; monitoring the quantum yields under photoirradiation at different wavelengths provided more mechanistic insight. As demonstrated in this work, keeping the same photon flux and reaction time (besides preparing the same chemical concentration and temperature) was a critical experimental condition to make a fair comparison of the quantum yields across different excitation wavelengths. It was found that leaching of Pd from the mesoporous Pd nanoparticles was not a major contribution to the observed catalytic activities. Eventually, the observed wavelength dependence of quantum yields was correlated with the wavelength dependence of the energy state of hot carriers, and a possible mechanism was proposed. This mechanism was overlooked in some previous studies (Han et al., 2017; Trinh et al., 2015; Xiao et al., 2014; Zhang et al., 2015), and it deserves more attention in utilizing hot carriers for catalysis.

RESULTS

Optical property and photocatalyzed condition of mesoporous Pd nanoparticles

Mesoporous Pd nanoparticles were prepared by a typical hard-template wet-chemical method, in which polystyrene-block-poly(ethylene oxide) and ascorbic acid acted as the template and the reductant, respectively (Li et al., 2019). The as-synthesized particles were cleaned by tetrahydrofuran (THF) and calcinated at 200°C for one hour to remove the solvent and most of the polymer, and the porous structure was still preserved (Li et al., 2019). The dry particles were further characterized and used as the catalyst. Fourier transform infrared spectroscopy (FTIR) did not detect any vibrational signal of organic compounds on the dry particles, indicating that the catalyst does not have much polymer left (Figure S1). Thermogravimetric analysis (TGA) confirmed that 22% of the dry particles' weight is the leftover polymer (Figure S2). The particles have an average hydrodynamic diameter of 79.9 $\pm$ 5.9 nm and a zeta potential of 0.6 mV when dispersed in water and measured by dynamic light scattering (DLS), a narrow size distribution of 63.3 $\pm$ 3.9 nm as determined by scanning electron microscopy (SEM) (Figures 1B and S3A), and an average pore size of 11.3 $\pm$ 3.3 nm (analyzing 100 pores in Figure 1C). The porous Pd nanoparticles had a large specific Brunauer-Emmett-Teller (BET) surface area of 57.1 m^2/g and an average pore size of 5.6 nm as determined by N_2 adsorption-desorption isotherms (See details in Figure S4). The particles have polycrystalline structures with grain sizes that are larger than the pore wall thickness(Li et al., 2019), and the pores form open channels throughout the particles as shown in a series of tilt transmission electron microscopy (TEM) images (Figure S5).

The mesoporous Pd nanoparticle solution has a broad UV-vis spectrum as compared to that of nonporous forms (Figure 1A).(Langhammer et al., 2006; Niu et al., 2008) For example, the nonporous 50 nm Pd nanoparticles (see a SEM image in Figure S3B) with a comparable mass to our catalysts have a broad absorption peak at 370 nm because of both plasmon resonance and interband transitions, but the absorption drops significantly in the red-photon and longer wavelength regions (Creighton and Eadon, 1991; Niu et al., 2008). In contrast, the porous particles' plasmon resonance absorption shifts significantly to these low energy regions, but the interband transitions stay in the UV-vis region because of the unchanged electronic structure of Pd (Figure 1A). Similarly, the mesoporous form of gold or platinum nanoparticles also shows significant red-shifts of plasmon resonances to the near infrared regions (Lu et al., 2020; Lv et al., 2019). The plasmonic coupling between either adjacent crystal domains or pore walls within proximity may be responsible for these red-shifts (Li et al., 2019; Liu et al., 2016). Thus, the optical absorbance of porous Pd nanoparticles in the 400-600 nm region focused in this study can only be assigned to interband transitions and the much longer wavelength region to plasmon resonance. On a drop-cast sample, the scattering intensity measured by an integrating sphere and a tunable laser follows approximately a $1/\lambda^4$ dependence, resembling Rayleigh scattering (Figure S6). Further measurement by a home-built setup for determining optical scattering and extinction on the colloidal solution in a 1 $\times$ 1cm quartz cuvette showed that the total light scattering in the range of 400 to 800 nm of the colloidal solution was almost negligible. Less than 3% of the incident photons were scattered from the photocatalyst and more than 97% were absorbed (Figure S7). From these results, it was concluded that the porous Pd nanoparticles had strong absorbance in the 400-600 nm region, and the dominant contribution to this absorbance is the interband transitions but not the plasmon resonance.

Suzuki–Miyaura reactions have been employed to evaluate the photocatalytic performance of Au–Pd alloy nanoparticles, or Pd nanoparticles loaded on metal oxides, or WS_2 (Raza et al., 2017; Sarina et al., 2014; Wang et al., 2013; Xiao et al., 2014). Besides the versatile applications of this reaction in creating C-C bonds and the transparent solutions of reactants and products for convenient photocatalysis study, the oxidative

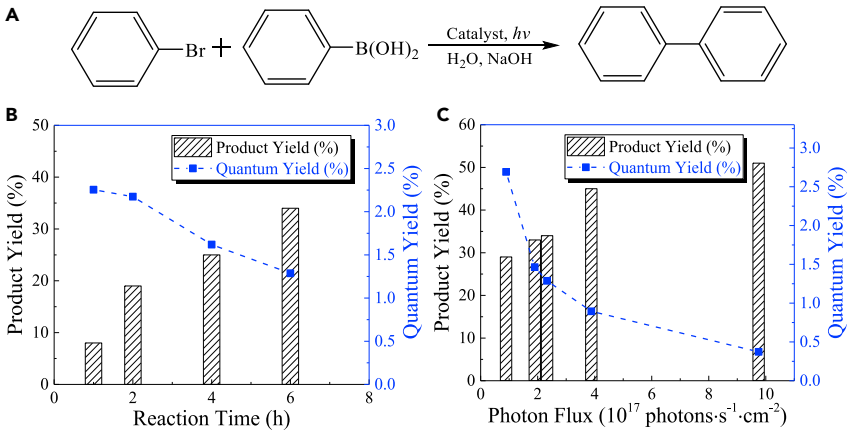

Figure 2. Suzuki–Miyaura C-C coupling reaction for evaluating photocatalytic performance of porous Pd nanoparticles

(A) Typical reaction process.

(B and C) Measured product yields (left axis) and quantum yields of the catalyst (right axis) under 405 nm LED irradiation with: (B) different reaction times under the same photon flux (around 2.4 × 10^{17} photon·s^{-1}·cm^{-2}), and (C) different photon fluxes under the same 6-h reaction. Small background product yields of the non-irradiated reactions with the catalyst were subtracted from the observed product yields when calculating the quantum yields.

addition of aryl halides (*i.e.*, the rate-determining step of the catalytic cycle) (Biffis et al., 2018) could be catalyzed by hot electrons generated from photo-exciting the Pd nanoparticle catalyst. In our typical reaction conditions at room temperature with different light-emitting diode (LED) light sources, bromobenzene and phenylboronic acid served as the coupling partners, sodium hydroxide as a base, and cetyltrimethylammonium chloride (CTAC) as a solubilizer to facilitate the dissolution of organic reactant and product into the aqueous solution (Figure 2A).(Sarina et al., 2014; Wang et al., 2013) The zeta potential of the porous Pd nanoparticle photocatalyst is around 60 mV in the reaction solution, which suggests some degree of adsorption of CTAC on the particles and explains for their high stability during the reaction. This DLS analysis also confirmed that the particles did not aggregate in the solution, and they maintained in colloidal form during the reaction. The biphenyl product was extracted from the reaction solution by dichloromethane and analyzed by proton nuclear magnetic resonance (^{1}H-NMR). The reaction time was purposely kept short enough to get a reasonable conversion range for reliable kinetic comparison (Sun et al., 2020), though a higher conversion was achieved with a longer reaction time.

The photothermal effect on the catalysis is neglectable in our experiment as local heating is minimal under continuous-wave irradiation and stirring (see more discussion in method details)(Mao et al., 2020; Nguyen et al., 2016). When considering the following processes after a colloidal metal nanoparticle in a stirring solution absorbs a single photon: (i) electron thermalization because of electron-electron and electron-phonon couplings (within few picoseconds (Link and El-Sayed, 2000; Minutella et al., 2017)), (ii) heat transfer from the particle to the local solvent (within 3 nanoseconds (Nguyen et al., 2016)), (iii) time gap for absorbing the second photon (about hundreds of nanoseconds), then it is obvious that the nanoparticle dissipates all the heat to the surrounding environment long before it absorbs the second photon. Because the hot carriers are well thermalized before the nanoparticle can transfer heat to the environment, it is reasonable to estimate the average temperature rise of the particle based on the energy of an absorbed photon, specific heat of Pd, and the particle's mass. This temperature rise is about 0.001°C under our experimental condition which should have no photothermal effect on our studied reaction. Under the constant stirring at high speed of the reaction solution, the transient heat in the LED beam path should be distributed evenly in the entire solution (Un and Sivan, 2021). The macroscopic temperature of reaction solutions rose only 1°C to 2°C as cooling fans were used. A UV-vis spectrum of reaction solution without the catalyst showed no obvious absorption at any wavelengths longer than 400 nm (Figure S8A). Blank tests on the reaction without the catalyst under different excitation wavelengths did not show any detectable product yield (Table S1). These control experiments confirmed that the light absorption of reactants could be ignored in our experiments, and the reaction under irradiation almost does not happen without the photocatalyst. It is worth noting that the reaction with the catalyst under the dark condition in 6 h gave a

background product yield of 5%. This background yield was subtracted from the product yields that were used to calculate quantum yields for the photocatalyzed reactions with 6-h irradiation. For photocatalyzed reactions with shorter irradiation times, the corresponding background yields were extrapolated from the ratios between the actual reaction times and 6 h. This extrapolation is reasonable for a very low conversion range where the reaction rate is assumed to be unchanged (Kozuch and Martin, 2012).

Establishing the same reaction time and photon flux for comparing of quantum yields of photocatalyst under various excitation wavelengths

Quantifying the efficiency of photocatalysts is an important criterion for practical application. This efficiency, here defined as the quantum yield of the catalyst, is calculated as the ratio of the number of product molecules to the number of absorbed photons. This quantity has two important benefits: it helps us understand the photocatalysis mechanism, and it establishes the effective cost of using photons for catalyzed chemical reactions. In practice, when monitoring a photocatalyzed reaction, the quantum yield of the photocatalyst is calculated as the number of product molecules produced per a specific time divided by the number of photons absorbed during that time. These two quantities can be extracted from the measured reaction rate and optical power absorbed by the photocatalyst. It is obvious that the reaction rate decreases as the reaction proceeds. Because the photon absorption rate is unchanged at any given time, the measured quantum yield, as defined above, is expected to be lower when the reaction happens for a longer time. To demonstrate this reasoning, the integrated reaction rates were measured (*i.e.*, total product molecules formed/total reaction time in seconds) when the reaction times were varied from 1 to 6 h under the same absorbed photon flux of a 405 nm LED. The quantum yields reduced from 2.3% to 1.3% (Figure 2B). The same trend was also observed under 490 nm LED irradiation (Table S2). This time-dependent behavior is similar to the case of using turn over frequency (TOF) to quantify the efficiency of catalysts under non-irradiated conditions. The measured TOF value always reduces as the catalyzed reaction proceeds, regardless of using homogeneous or heterogeneous catalysts(Kozuch and Martin, 2012; Lente, 2013). The TOF does not entirely reflect the kinetics of a catalyzed reaction, and the rate law should be the better description (Lente, 2013). In our study, because we wanted to compare quantum yields of the photocatalyst under various excitation wavelengths, we did not need to derive a rate law of our photocatalyzed reaction under each excitation wavelength. However, we did need to have the photocatalyzed reactions run for the same time interval when comparing quantum yields of the catalyst under different excitations. Another option (but less practical under our experimental conditions) is to compare quantum yields when keeping the same conversion (or product yield) of these reactions, which eventually will give us the same trend of quantum yields as in the case of keeping the same reaction time.

Using a similar argument based on chemical kinetics as mentioned above, a higher photon flux condition creates more photoexcited nanoparticles, and effectively causes higher product yield and lower reactant concentration. As the reaction proceeds, each nanoparticle catalyst encounters a decreasing concentration of reactants, and the efficiency of extracting hot carriers is reduced, hence the quantum yield will be effectively reduced. Using the same reaction condition with 405 nm LED irradiation and 6 h reaction time for comparison, when the photon flux increases from 0.9×10^{17} to 9.8×10^{17} photon$\cdot s^{-1}\cdot cm^{-2}$, the measured quantum yield decreases from 2.7% to 0.4% (Figure 2C). A similar trend was observed with 470 nm LED irradiation (Table S3). To recap, when comparing the quantum yields of the photocatalyst under different irradiation conditions, we should not only keep the same starting experimental condition but also the exact same reaction time and photon flux. This prerequisite is critical for revealing the photocatalytic mechanism in the next section.

Wavelength dependence of photocatalytic activities and proposed catalytic mechanism

Before moving into the comparison of quantum yields at different excitation wavelengths, we want to examine any catalytic mechanism other than the hot carriers induced photocatalysis mechanism. It is known that leaching of Pd atoms from nanostructures into the reaction solution may complicate the catalytic mechanism (Xiao et al., 2014) (Costa et al., 2020; Phan et al., 2006; Sun et al., 2020). In our hot filtration tests (Scheme S3), the photocatalyzed reactions were allowed to proceed for one hour followed by the removal of nanoparticles from the reaction solution via centrifugation, and then the reactions were allowed to continue for another 5 h before determining the product yields. These product yields were much lower than those of full reactions with 6-h irradiation (Table S5) but were higher than the yields of control experiments in which the photocatalyzed reactions were only let to react for one hour and the product yield was determined immediately. The UV-vis spectra of the supernatants after 1 h reaction (Figure S9) did not

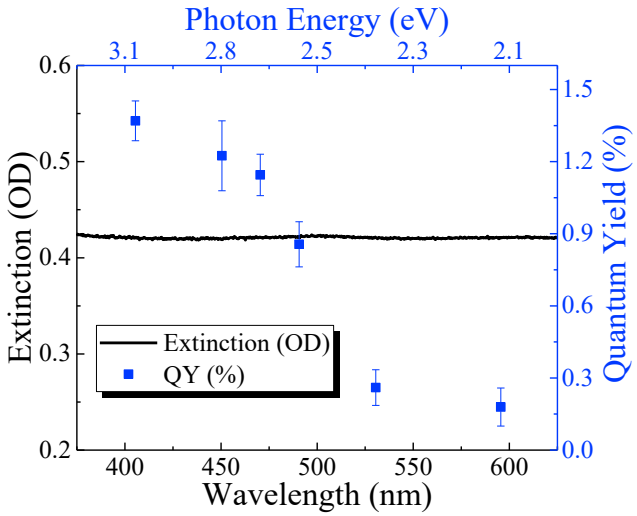

Figure 3. Photocatalysis of porous Pd nanoparticles for Suzuki–Miyaura C-C coupling reaction

Wavelength dependence of quantum yields (right axis) and the optical spectrum of reaction solution with porous Pd nanoparticles (left axis) for comparison. Each error bar is one standard deviation of the mean. See also Table S4.

exhibit any noticeable features of $[PdCl_4]^{2-}$ complex (Figure S8B) or the mesoporous Pd nanoparticles. These results indicate that the supernatants from hot filtration have little leached Pd that can also catalyze the reaction, and the contribution of leached Pd to the observed catalysis is small. In addition, the above result is also consistent with other studies under similar reaction conditions using Au–Pd alloy nanoparticle photocatalyst loaded on ZrO_2(Cong and Porco, 2012; Xiao et al., 2014). More importantly, this contribution did not exhibit clear wavelength dependence in our experiments (Table S5). Furthermore, inductively coupled plasma optical emission spectroscopic (ICP-OES) analysis for Pd in the supernatants of the 6-h reactions under either dark or irradiation conditions showed that the amount of Pd was under detection limit, thus the utmost Pd leached based on the detection limit was estimated to be about 1.2% of the total Pd in the nanoparticle photocatalyst (See details in Figure S10 and Table S10). Although the chemical structure or formula of this leached Pd species is still unknown and not the focus of this study, another control reaction using $PdCl_2$ as the pre-catalyst (the source of generating Pd(0) for the catalytic cycle) showed no wavelength dependence of the product yields (Figure S11). This test indicates that the complete catalytic cycle of the molecular Pd catalyst does not depend on any tested wavelengths. Lastly, X-ray photoelectron spectroscopy (XPS) showed no distinct changes of the oxidation state of Pd(0) in porous Pd nanoparticles before and after reactions in the dark and photocatalyzed conditions (Table S11 and Figure S12). Overall, it is clear that the photoexcited Pd nanoparticles, hence the hot electrons and holes generated in the particles, are the key catalysts of the studied reaction, and the wavelength dependence of quantum yields must be attributed to the different states of hot carriers generated by different excitation wavelengths.

In experiments determining the wavelength dependence of quantum yields of the catalyst, the same absorbed photon flux (around 2.4×10^{17} photon$\cdot s^{-1}\cdot cm^{-2}$) and reaction time (6 h) were maintained for each excitation wavelength. Interestingly, the quantum yields do not track the extinction spectrum of porous Pd nanoparticles (Figure 3). Indeed, the quantum yields are much higher in the shorter wavelength region. To explain this observation, it is important to correlate this wavelength-dependent trend with the state of hot holes and electrons generated in the porous Pd nanoparticles at different excitation wavelengths. It is known that each interband transition in *d*-block metals generates a pair of hot electron and hole, in which the hot electron resides near the Fermi level, and the hot hole resides in the *d*-band. When shorter wavelength photons are absorbed, the holes reside at much lower energy states or "deeper" in the *d*-band, but the electrons remain almost the same energy just above the Fermi level (Christopher and Moskovits, 2017; Khurgin, 2020; Weaver and Benbow, 1975). Thus, a possible photocatalytic mechanism was proposed in Figure 4, emphasizing on the role of deeper hot holes with stronger oxidizing power for accelerating the oxidative addition step of aryl halide, a rate determining step in the C-C coupling catalytic cycle (Biffis et al., 2018). In other words, deeper holes have much lower energy than Fermi level, and the lowest possible energy (as compared to vacuum level) is $E^{NP}_{hole}(eV) = E^{NP}_F - h\nu$. The reduction potential

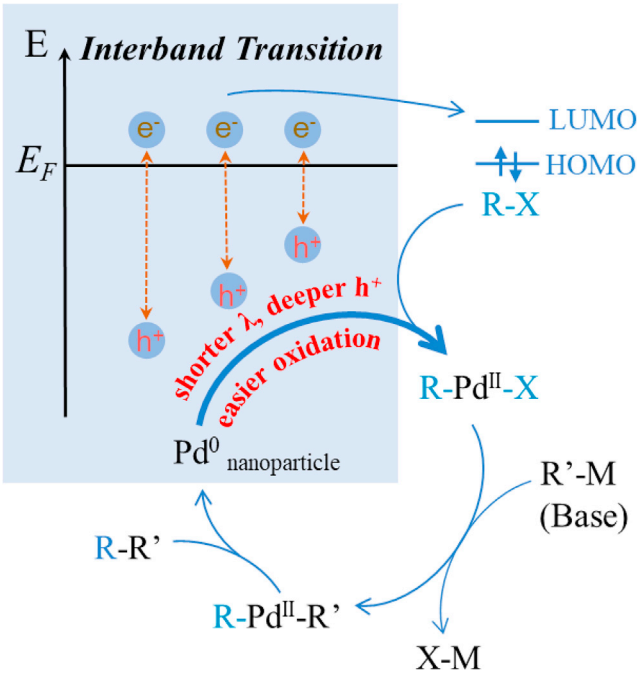

Figure 4. Proposed mechanism

Proposed photocatalytic mechanism of hot holes in accelerating the oxidative addition, a rate-determining step of the catalytic cycle

of Pd(II)/Pd(0) for the nanoparticle photocatalyst under the influence of these holes, $E^{NP-hole}_{Pd(II)/Pd(0)}$ (V *vs* SHE), can be determined by this relationship: $E^{NP}_{hole} = -4.44\ eV + eE^{NP-hole}_{Pd(II)/Pd(0)}$(Mao et al., 2020; Reiss, 1985). Thus, deeper holes lower the reduction potential of Pd(II)/Pd(0) and favor the oxidation of Pd on the nanoparticle catalyst. Thus, more R-Pd^{II}-X intermediates are produced, and eventually the reaction yields and the quantum yields increase. Direct detection of R-Pd^{II}-X intermediates is still a challenge (Chen et al., 2018); however, the deeper hot holes have been observed to catalyze the oxidation of metal nanoparticles better (Al-Zubeidi et al., 2019; Saito et al., 2016; Zhao et al., 2017). Thus, the oxidative addition step in this study must be catalyzed by the hot holes. Figure 3 shows that the quantum yield starts to pick up at around the 530 nm region and increases drastically around the 490 nm region, resembling a step-function-like dependence of the quantum yields to the excitation wavelengths. This behavior suggests a threshold of photon energy is needed to overcome the barrier of the oxidative addition reaction.

The crucial role of hot holes involved in the oxidative addition step was further confirmed by adding a hole scavenger, isopropanol, to the reaction. Under different excitation wavelengths, the product yields were quite close to that of a non-irradiated reaction (Table S6). This result can be explained by the fact that isopropanol is a stronger reducing agent (E^o of acetone/isopropanol is around 0.76 V *vs* SHE) (Waidhas et al., 2020) than Pd (E^o of Pd(II)/Pd(0) is around 0.92 V *vs* SHE) (Bratsch, 1989), and that the holes are quenched by isopropanol before they can catalyze the formation of R-Pd^{II}-X intermediate. To address the concern of homocoupling of phenylboronic acid (Adamo et al., 2006) that could be catalyzed by the hot holes (Gellé et al., 2020) or bromobenzene to the biphenyl, a series of control experiments using only either reactant showed undetected product under various irradiation conditions (Table S7). Other control experiments with 4-bromoanisole and phenylboronic acid under the dark and 405 nm irradiation conditions confirmed that hetero-coupled 4-methoxy-1,1′-biphenyl was the only product (see details in method details). In addition, some other possible side reactions including deborylation, debromination, or substitution by hydroxyl group of the reactants were neglectable as compared to the formation of the biphenyl product as confirmed by gas chromatography-mass spectrometry (GC-MS, see details in method details and supplemental information). Moreover, as we mentioned in our hot filtration tests, the leaching of Pd atoms (in the form of molecular Pd species) has a very small contribution to the observed product yield, thus the R-Pd^{II}-X intermediate catalyzed by hot holes is likely to stay on the nanoparticle surface, and the consequent catalytic steps (*e.g.*, transmetallation, reductive elimination) may happen on this surface, as suggested by other studies (Biffis et al., 2018; Pérez-Lorenzo, 2012).

Our proposed mechanism provides another insight into the role of deep holes in the photocatalysis of Pd nanoparticles. A previous work using nonporous Pd nanoparticles on ZrO_2 powder concluded that hot electrons played a decisive role in the oxidation addition step. It was proposed that the shorter excitation wavelengths generated higher energy electrons because of interband transitions, and the hotter electrons catalyzed the oxidative addition step better (Sarina et al., 2014). In fact, as we discussed above, the general physical picture of shorter-wavelength excitation in the interband transition regime is the hot electrons reside near the Fermi level, and hot holes reside deeper in the *d*-band (Christopher and Moskovits, 2017; Khurgin, 2020; Weaver and Benbow, 1975). Thus, the observed wavelength dependence of the quantum yields in that experiment could be explained by the stronger oxidizing power of the hot holes in the deeper *d*-band, as suggested in Figure 4. The hot electrons near the Fermi level may activate the aryl halide by promoting electron transfer from the metal to the LUMO of the aryl halide, but this step (hence the hot electron induced mechanism) should not show a strong wavelength dependence in the interband transition regime.

DISCUSSION

The wavelength dependence of quantum yield or reaction yield of similar C-C coupling reactions was also observed in other photocatalysts (Gellé et al., 2020), such as Au-Pd alloy nanoparticles supported on ZrO_2 (Xiao et al., 2014) or Pd nanoparticles decorated on gold nanorods (Wang et al., 2013). However, the role of hot holes generated from interband transitions was not fully explored yet. It is important to mention that our porous Pd nanoparticle photocatalyst has several advantages of revealing the photocatalytic mechanism, such as the suppression of plasmon resonance and the dominant contribution of interband transitions in the optical region studied, a very low light scattering for determining quantum yield with high accuracy, and no interference of supporting materials to the photocatalytic interpretation. Furthermore, our catalyst does show a higher photocatalytic efficiency as compared to the nonporous Pd nanoparticles and some other catalysts under similar experimental conditions (see comparison in Table S8), probably because the porous structure increases the probability of hot carrier diffusion to the catalyst's surface (Huang et al., 2020; Mao et al., 2019; Wang et al., 2012). It is known that the hot holes have smaller kinetic energy and shorter mean free path than electrons do (Khurgin, 2020), thus the porous structure may overcome these obstacles.

In summary, the interband transitions of porous Pd nanoparticles were examined to reveal the wavelength-dependent quantum yields of a prototype C-C coupling reaction. With shorter excitation wavelengths, the deeper holes in the *d*-band with stronger oxidizing power can catalyze the oxidative addition of aryl halide R-X onto Pd^0 better to form more R-Pd^{II}-X intermediates in the catalytic cycle, thus the quantum yield of the catalyst increases. It is known that the oxidative addition process can be catalyzed by hot electrons, especially electrons with high kinetic energy generated from plasmon resonance (Sarina et al., 2014; Wang et al., 2013; Xiao et al., 2014). However, we showed here that interband transitions could also catalyze the oxidation reaction by another process: the strong oxidizing holes can also promote the oxidation of Pd^0 to Pd^{II}. We hope this work will prompt more interest in utilizing deep holes from interband transitions for higher photocatalytic efficiency, which has recently picked up some attention (Al-Zubeidi et al., 2019; Tagliabue et al., 2018, 2020; Yu et al., 2019).

Limitations of the study

Deeper holes generated from interband transitions catalyzing Suzuki-Miyaura reactions better was demonstrated by using porous Pd nanoparticle photocatalysts. However, direct evidence of the catalytic process, such as *in situ* detection of R-Pd^{II}-X intermediates or experimental measurement of reduction potential of hot holes, is needed to further strengthen the conclusion. A comprehensive comparison between interband transitions and plasmon resonance in photocatalysis should be studied in future work.

STAR★METHODS

Detailed methods are provided in the online version of this paper and include the following:

- KEY RESOURCES TABLE
- RESOURCE AVAILABILITY
  - Lead contact
  - Materials availability
  - Data and code availability

SUPPLEMENTAL INFORMATION

Supplemental information can be found online at https://doi.org/10.1016/j.isci.2022.103737.

ACKNOWLEDGMENTS

The authors would like to thank Duy Nguyen for her fruitful discussions, Anne Pham from the Molecular Foundry of the Lawrence Berkeley National Laboratory and Professor Jennifer Lu from UC Merced for providing technical support for TGA measurements, Professor Peggy A. O'Day for nitrogen gas sorption measurements, and Dr. Liying Zhao from UC Merced for ICP-OES measurements. R. E. acknowledges the research fellowship from Merced Nanomaterials Center for Energy and Sensing (funded by NASA grant no. NNX15AQ01A).

AUTHOR CONTRIBUTIONS

S.C.N. and S.G. jointly supervised this work. P.L. designed and carried out the experiments. R.E. synthesized the nonporous Pd nanoparticles. M.I.K. measured the light scattering of the drop-cast mesoporous Pd nanoparticles. W.C.S. helped with the organic reactions and revision of manuscript. All authors discussed the results and prepared the manuscript.

DECLARATION OF INTERESTS

The authors declare no competing interests.

Received: October 11, 2021
Revised: November 17, 2021
Accepted: December 30, 2021
Published: February 18, 2022

REFERENCES

Adamo, C., Amatore, C., Ciofini, I., Jutand, A., and Lakmini, H. (2006). Mechanism of the Palladium-catalyzed homocoupling of arylboronic acids:key involvement of a palladium peroxo complex. J. Am. Chem. Soc. *128*, 6829–6836. https://doi.org/10.1021/ja0569959.

Al-Zubeidi, A., Hoener, B.S., Collins, S.S.E., Wang, W., Kirchner, S.R., Hosseini Jebeli, S.A., Joplin, A., Chang, W.-S., Link, S., and Landes, C.F. (2019). Hot holes assist plasmonic nanoelectrode dissolution. Nano Lett. *19*, 1301–1306. https://doi.org/10.1021/acs.nanolett.8b04894.

Aslam, U., Rao, V.G., Chavez, S., and Linic, S. (2018). Catalytic conversion of solar to chemical energy on plasmonic metal nanostructures. Nat. Catal. *1*, 656–665. https://doi.org/10.1038/s41929-018-0138-x.

Balajka, J., Hines, M.A., DeBenedetti, W.J.I., Komora, M., Pavelec, J., Schmid, M., and Diebold, U. (2018). High-affinity adsorption leads to molecularly ordered interfaces on TiO_2 in air and solution. Science *361*, 786. https://doi.org/10.1126/science.aat6752.

Bernardi, M., Mustafa, J., Neaton, J.B., and Louie, S.G. (2015). Theory and computation of hot carriers generated by surface plasmon polaritons in noble metals. Nat. Commun. *6*, 7044. https://doi.org/10.1038/ncomms8044.

Biffis, A., Centomo, P., Del Zotto, A., and Zecca, M. (2018). Pd metal catalysts for cross-couplings and related reactions in the 21st century: a critical review. Chem. Rev. *118*, 2249–2295. https://doi.org/10.1021/acs.chemrev.7b00443.

Boltersdorf, J., Forcherio, G.T., McClure, J.P., Baker, D.R., Leff, A.C., and Lundgren, C. (2018). Visible light-promoted plasmon resonance to induce "hot" hole transfer and photothermal conversion for catalytic oxidation. J. Phys. Chem. C *122*, 28934–28948. https://doi.org/10.1021/acs.jpcc.8b09248.

Bratsch, S.G. (1989). Standard electrode potentials and temperature coefficients in water at 298.15 K. J. Phys. Chem. Ref. Data *18*, 1–21. https://doi.org/10.1063/1.555839.

Brus, L. (2008). Noble metal nanocrystals: plasmon electron transfer photochemistry and single-molecule Raman spectroscopy. Acc. Chem. Res. *41*, 1742–1749. https://doi.org/10.1021/ar800121r.

Chang, L., Besteiro, L.V., Sun, J.C., Santiago, E.Y., Gray, S.K., Wang, Z.M., and Govorov, A.O. (2019). Electronic structure of the plasmons in metal nanocrystals: fundamental limitations for the

energy efficiency of hot electron generation. ACS Energy Lett. *4*, 2552–2568. https://doi.org/10.1021/acsenergylett.9b01617.

Chastain, J., and King, R.C., Jr. (1992). Handbook of X-ray photoelectron spectroscopy, *40* (Perkin-Elmer Corporation), p. 221.

Chen, Z., Vorobyeva, E., Mitchell, S., Fako, E., Ortuño, M.A., López, N., Collins, S.M., Midgley, P.A., Richard, S., Vilé, G., and Pérez-Ramírez, J. (2018). A heterogeneous single-atom palladium catalyst surpassing homogeneous systems for Suzuki coupling. Nat. Nanotechnol. *13*, 702–707. https://doi.org/10.1038/s41565-018-0167-2.

Christopher, P., and Moskovits, M. (2017). Hot charge carrier transmission from plasmonic nanostructures. Annu. Rev. Phys. Chem. *68*, 379–398. https://doi.org/10.1146/annurev-physchem-052516-044948.

Christopher, P., Xin, H., and Linic, S. (2011). Visible-light-Enhanced catalytic oxidation reactions on plasmonic silver nanostructures. Nat. Chem. *3*, 467–472. https://doi.org/10.1038/nchem.1032.

Cong, H., and Porco, J.A. (2012). Chemical synthesis of complex molecules using nanoparticle catalysis. ACS. Catal. *2*, 65–70. https://doi.org/10.1021/cs200495s.

Costa, P., Sandrin, D., and Scaiano, J.C. (2020). Real-time fluorescence imaging of a heterogeneously catalysed suzuki–miyaura reaction. Nat. Catal. *3*, 427–437. https://doi.org/10.1038/s41929-020-0442-0.

Creighton, J.A., and Eadon, D.G. (1991). Ultraviolet–visible absorption spectra of the colloidal metallic elements. J. Chem. Soc. Faraday Trans. *87*, 3881–3891. https://doi.org/10.1039/FT9918703881.

Deng, Y., Yu, T., Wan, Y., Shi, Y., Meng, Y., Gu, D., Zhang, L., Huang, Y., Liu, C., and Wu, X. (2007). Ordered mesoporous silicas and carbons with large accessible pores templated from amphiphilic diblock copolymer poly(ethylene oxide)-b-polystyrene. J. Am. Chem. Soc. *129*, 1690–1697. https://doi.org/10.1021/ja067379v.

Dubi, Y., Un, I.W., and Sivan, Y. (2020). Thermal effects – an alternative mechanism for plasmon-assisted photocatalysis. Chem. Sci. *11*, 5017–5027. https://doi.org/10.1039/C9SC06480J.

DuChene, J.S., Tagliabue, G., Welch, A.J., Cheng, W.H., and Atwater, H.A. (2018). Hot hole collection and photoelectrochemical CO_2 reduction with plasmonic Au/p-GaN photocathodes. Nano Lett. *18*, 2545–2550. https://doi.org/10.1021/acs.nanolett.8b00241.

Fu, Z., Li, T., He, X., Liu, J., and Wu, Y. (2014). The recyclable cyclopalladated ferrocenylimine self-assembly catalytic film and investigation of its role in the mechanism of heterogeneous catalysis. RSC. Adv. *4*, 26413–26420. https://doi.org/10.1039/C4RA02540G.

Fujishima, A., Zhang, X., and Tryk, D.A. (2008). TiO_2 photocatalysis and related surface phenomena. Surf. Sci. Rep. *63*, 515–582. https://doi.org/10.1016/j.surfrep.2008.10.001.

Gellé, A., Jin, T., de la Garza, L., Price, G.D., Besteiro, L.V., and Moores, A. (2020). Applications of plasmon-enhanced nanocatalysis to organic transformations. Chem. Rev. *120*, 986–1041. https://doi.org/10.1021/acs.chemrev.9b00187.

Gniewek, A., Trzeciak, A.M., Ziółkowski, J.J., Kępiński, L., Wrzyszcz, J., and Tylus, W. (2005). Pd-PVP colloid as catalyst for heck and carbonylation reactions: TEM and XPS studies. J. Catal. *229*, 332–343. https://doi.org/10.1016/j.jcat.2004.11.003.

Guerrisi, M., Rosei, R., and Winsemius, P. (1975). Splitting of the interband Absorption edge in Au. Phys. Rev. B *12*, 557–563. https://doi.org/10.1103/PhysRevB.12.557.

Han, D., Bao, Z., Xing, H., Yang, Y., Ren, Q., and Zhang, Z. (2017). Fabrication of plasmonic Au–Pd alloy nanoparticles for photocatalytic suzuki–miyaura reactions under ambient conditions. Nanoscale *9*, 6026–6032. https://doi.org/10.1039/C7NR01950E.

He, G.S., Qin, H.-Y., and Zheng, Q. (2009). Rayleigh, mie, and tyndall scatterings of polystyrene microspheres in water: wavelength, size, and angle dependences. J. Appl. Phys. *105*, 023110. https://doi.org/10.1063/1.3068473.

Hou, W., and Cronin, S.B. (2013). A review of surface plasmon resonance-enhanced photocatalysis. Adv. Funct. Mater. *23*, 1612–1619. https://doi.org/10.1002/adfm.201202148.

Hou, W., Hung, W.H., Pavaskar, P., Goeppert, A., Aykol, M., and Cronin, S.B. (2011). Photocatalytic conversion of CO_2 to hydrocarbon fuels via plasmon-enhanced absorption and metallic interband transitions. ACS. Catal. *1*, 929–936. https://doi.org/10.1021/cs2001434.

Huang, S.-C., Wang, X., Zhao, Q.-Q., Zhu, J.-F., Li, C.-W., He, Y.-H., Hu, S., Sartin, M.M., Yan, S., and Ren, B. (2020). Probing nanoscale spatial distribution of plasmonically excited hot carriers. Nat. Commun. *11*, 4211. https://doi.org/10.1038/s41467-020-18016-4.

Huang, Y.M., Liu, Z., Gao, G.P., Xiao, Q., Martens, W., Du, A.J., Sarina, S., Guo, C., and Zhu, H.Y. (2018). Visible light-driven selective hydrogenation of unsaturated aromatics in an aqueous solution by direct photocatalysis of Au nanoparticles. Catal. Sci. Technol. *8*, 726–734. https://doi.org/10.1039/c7cy02291c.

Iatridi, Z., Evangelatou, K., Theodorakis, N., Angelopoulou, A., Avgoustakis, K., and Tsitsilianis, C. (2020). Multicompartmental mesoporous silica/polymer nanostructured hybrids: design capabilities by integrating linear and star-shaped block copolymers. Polymers *12*, 51. https://doi.org/10.3390/polym12010051.

Iqbal, M., Li, C., Jiang, B., Hossain, M.S.A., Islam, M.T., Henzie, J., and Yamauchi, Y. (2017). Tethering mesoporous Pd nanoparticles to reduced graphene oxide sheets forms highly efficient electrooxidation catalysts. J. Mater. Chem. A. *5*, 21249–21256. https://doi.org/10.1039/C7TA05091G.

Jain, P.K. (2019). Taking the heat off of plasmonic chemistry. J. Phys. Chem. C *123*, 24347–24351. https://doi.org/10.1021/acs.jpcc.9b08143.

Kazuma, E., and Kim, Y. (2019). Mechanistic studies of plasmon chemistry on metal catalysts. Angew. Chem. Int. Ed. *58*, 4800–4808. https://doi.org/10.1002/anie.201811234.

Khurgin, J.B. (2020). Fundamental limits of hot carrier injection from metal in nanoplasmonics. Nanophotonics *9*, 453–471. https://doi.org/10.1515/nanoph-2019-0396.

Kim, Y., Dumett Torres, D., and Jain, P.K. (2016). Activation energies of plasmonic catalysts. Nano Lett. *16*, 3399–3407. https://doi.org/10.1021/acs.nanolett.6b01373.

Kim, Y., Smith, J.G., and Jain, P.K. (2018). Harvesting multiple electron-hole pairs generated through plasmonic excitation of Au nanoparticles. Nat. Chem. *10*, 763–769. https://doi.org/10.1038/s41557-018-0054-3.

Kontoleta, E., Tsoukala, A., Askes, S.H.C., Zoethout, E., Oksenberg, E., Agrawal, H., and Garnett, E.C. (2020). Using hot electrons and hot holes for simultaneous cocatalyst deposition on plasmonic nanostructures. ACS. Appl. Mater. Inter. *12*, 35986–35994. https://doi.org/10.1021/acsami.0c04941.

Kozuch, S., and Martin, J.M.L. (2012). "Turning over" definitions in catalytic cycles. ACS. Catal. *2*, 2787–2794. https://doi.org/10.1021/cs3005264.

Langhammer, C., Yuan, Z., Zorić, I., and Kasemo, B. (2006). Plasmonic properties of supported Pt and Pd nanostructures. Nano Lett. *6*, 833–838. https://doi.org/10.1021/nl060219x.

Lente, G. (2013). Comment on "'Turning over' definitions in catalytic cycles". ACS. Catal. *3*, 381–382. https://doi.org/10.1021/cs300846b.

Li, C., Iqbal, M., Jiang, B., Wang, Z., Kim, J., Nanjundan, A.K., Whitten, A.E., Wood, K., and Yamauchi, Y. (2019). Pore-tuning to boost the electrocatalytic activity of polymeric micelle-templated mesoporous Pd nanoparticles. Chem. Sci. *10*, 4054–4061. https://doi.org/10.1039/C8SC03911A.

Linic, S., Christopher, P., and Ingram, D.B. (2011). Plasmonic-metal nanostructures for efficient conversion of solar to chemical energy. Nat. Mater. *10*, 911–921. https://doi.org/10.1038/nmat3151.

Link, S., and El-Sayed, M.A. (2000). Shape and size dependence of radiative, non-radiative and photothermal properties of gold nanocrystals. Int. Rev. Phys. Chem. *19*, 409–453. https://doi.org/10.1080/01442350050034180.

Liu, B.-J., Lin, K.-Q., Hu, S., Wang, X., Lei, Z.-C., Lin, H.-X., and Ren, B. (2015). Extraction of absorption and scattering contribution of metallic nanoparticles toward rational synthesis and application. Anal. Chem. *87*, 1058–1065. https://doi.org/10.1021/ac503612b.

Liu, K., Bai, Y., Zhang, L., Yang, Z., Fan, Q., Zheng, H., Yin, Y., and Gao, C. (2016). Porous Au–Ag nanospheres with high-density and highly accessible hotspots for SERS analysis. Nano Lett. *16*, 3675–3681. https://doi.org/10.1021/acs.nanolett.6b00868.

Liu, L., Li, P., Adisak, B., Ouyang, S., Umezawa, N., Ye, J., Kodiyath, R., Tanabe, T., Ramesh, G.V., Ueda, S., and Abe, H. (2014). Gold

photosensitized $SrTiO_3$ for visible-light water oxidation induced by Au interband transitions. J. Mater. Chem. A *2*, 9875–9882. https://doi.org/10.1039/C4TA01988A.

Lu, Z., Gao, J., Fang, C., Zhou, Y., Li, X., and Han, G. (2020). Porous Pt nanospheres incorporated with GO_x to enable synergistic oxygen-inductive starvation/electrodynamic tumor therapy. Adv. Sci. *7*, 2001223. https://doi.org/10.1002/advs.202001223.

Lv, H., Xu, D., Henzie, J., Feng, J., Lopes, A., Yamauchi, Y., and Liu, B. (2019). Mesoporous gold nanospheres via thiolate–Au(i) intermediates. Chem. Sci. *10*, 6423–6430. https://doi.org/10.1039/C9SC01728C.

Mao, Z., Espinoza, R., Garcia, A., Enwright, A., Vang, H., and Nguyen, S.C. (2020). Tuning redox potential of gold nanoparticle photocatalysts by light. ACS Nano *14*, 7038–7045. https://doi.org/10.1021/acsnano.0c01704.

Mao, Z., Vang, H., Garcia, A., Tohti, A., Stokes, B.J., and Nguyen, S.C. (2019). Carrier diffusion—the main contribution to size-dependent photocatalytic activity of colloidal gold nanoparticles. ACS. Catal. *9*, 4211–4217. https://doi.org/10.1021/acscatal.9b00390.

Minutella, E., Schulz, F., and Lange, H. (2017). Excitation-dependence of plasmon-induced hot electrons in gold nanoparticles. J. Phys. Chem. Lett. *8*, 4925–4929. https://doi.org/10.1021/acs.jpclett.7b02043.

Molnár, Á. (2011). Efficient, selective, and recyclable palladium catalysts in Carbon−Carbon coupling reactions. Chem. Rev. *111*, 2251–2320. https://doi.org/10.1021/cr100355b.

Mukherjee, S., Libisch, F., Large, N., Neumann, O., Brown, L.V., Cheng, J., Lassiter, J.B., Carter, E.A., Nordlander, P., and Halas, N.J. (2013). Hot electrons do the impossible: plasmon-induced dissociation of H_2 on Au. Nano Lett. *13*, 240–247. https://doi.org/10.1021/nl303940z.

Nguyen, S.C., Zhang, Q., Manthiram, K., Ye, X., Lomont, J.P., Harris, C.B., Weller, H., and Alivisatos, A.P. (2016). Study of heat transfer dynamics from gold nanorods to the environment via time-resolved infrared spectroscopy. ACS Nano *10*, 2144–2151. https://doi.org/10.1021/acsnano.5b06623.

Niu, W., Li, Z.-Y., Shi, L., Liu, X., Li, H., Han, S., Chen, J., and Xu, G. (2008). Seed-mediated growth of nearly monodisperse palladium nanocubes with controllable sizes. Cryst. Growth Des. *8*, 4440–4444. https://doi.org/10.1021/cg8002433.

Pérez-Lorenzo, M. (2012). Palladium nanoparticles as efficient catalysts for Suzuki cross-coupling reactions. J. Phys. Chem. Lett. *3*, 167–174. https://doi.org/10.1021/jz2013984.

Phan, N.T.S., VanDerSluys, M., and Jones, C.W. (2006). On the nature of the active species in palladium catalyzed mizoroki –heckand Suzuki –MiyauraCouplings –homogeneousor heterogeneous catalysis ,ACritical review. Adv. Synth. Catal. *348*, 609–679. https://doi.org/10.1002/adsc.200505473.

Raza, F., Yim, D., Park, J.H., Kim, H.-I., Jeon, S.-J., and Kim, J.-H. (2017). Structuring Pd nanoparticles on 2H-WS_2 nanosheets induces excellent photocatalytic activity for cross-coupling reactions under visible light. J. Am. Chem. Soc. *139*, 14767–14774. https://doi.org/10.1021/jacs.7b08619.

Reiss, H. (1985). The Fermi level and the redox potential. J. Phys. Chem. *89*, 3783–3791. https://doi.org/10.1021/j100264a005.

Saito, K., Tanabe, I., and Tatsuma, T. (2016). Site-selective plasmonic etching of silver nanocubes. J. Phys. Chem. Lett. *7*, 4363–4368. https://doi.org/10.1021/acs.jpclett.6b02393.

Sakamoto, H., Ohara, T., Yasumoto, N., Shiraishi, Y., Ichikawa, S., Tanaka, S., and Hirai, T. (2015). Hot-electron-induced highly efficient O_2 activation by Pt nanoparticles supported on Ta_2O_5 driven by visible light. J. Am. Chem. Soc. *137*, 9324–9332. https://doi.org/10.1021/jacs.5b04062.

Sarina, S., Zhu, H.-Y., Xiao, Q., Jaatinen, E., Jia, J., Huang, Y., Zheng, Z., and Wu, H. (2014). Viable photocatalysts under solar-spectrum irradiation: nonplasmonic metal nanoparticles. Angew. Chem. Int. Ed. *53*, 2935–2940. https://doi.org/10.1002/anie.201308145.

Seemala, B., Therrien, A.J., Lou, M.H., Li, K., Finzel, J.P., Qi, J., Nordlander, P., and Christopher, P. (2019). Plasmon-mediated catalytic O_2 dissociation on Ag nanostructures: hot electrons or near fields? ACS Energy Lett. *4*, 1803–1809. https://doi.org/10.1021/acsenergylett.9b00990.

Sun, B., Ning, L., and Zeng, H.C. (2020). Confirmation of suzuki–miyaura cross-coupling reaction mechanism through synthetic architecture of nanocatalysts. J. Am. Chem. Soc. *142*, 13823–13832. https://doi.org/10.1021/jacs.0c04804.

Sundararaman, R., Narang, P., Jermyn, A.S., Goddard, W.A., III, and Atwater, H.A. (2014). Theoretical predictions for hot-carrier generation from surface plasmon decay. Nat. Commun. *5*, 5788. https://doi.org/10.1038/ncomms6788.

Tagliabue, G., DuChene, J.S., Abdellah, M., Habib, A., Gosztola, D.J., Hattori, Y., Cheng, W.-H., Zheng, K., Canton, S.E., Sundararaman, R., et al. (2020). Ultrafast hot-hole injection modifies hot-electron dynamics in Au/p-GaN heterostructures. Nat. Mater. *19*, 1312–1318. https://doi.org/10.1038/s41563-020-0737-1.

Tagliabue, G., Jermyn, A.S., Sundararaman, R., Welch, A.J., DuChene, J.S., Pala, R., Davoyan, A.R., Narang, P., and Atwater, H.A. (2018). Quantifying the role of surface plasmon excitation and hot carrier transport in plasmonic devices. Nat. Commun. *9*, 3394. https://doi.org/10.1038/s41467-018-05968-x.

Trinh, T.T., Sato, R., Sakamoto, M., Fujiyoshi, Y., Haruta, M., Kurata, H., and Teranishi, T. (2015). Visible to near-infrared plasmon-enhanced catalytic activity of Pd hexagonal nanoplates for the Suzuki coupling reaction. Nanoscale *7*, 12435–12444. https://doi.org/10.1039/C5NR03841C.

Un, I.-W., and Sivan, Y. (2021). The role of heat generation and fluid flow in plasmon-enhanced reduction–oxidation reactions. ACS Photon. *8*. https://doi.org/10.1021/acsphotonics.1c00113.

Waidhas, F., Haschke, S., Khanipour, P., Fromm, L., Görling, A., Bachmann, J., Katsounaros, I., Mayrhofer, K.J.J., Brummel, O., and Libuda, J. (2020). Secondary alcohols as rechargeable electrofuels: electrooxidation of isopropyl alcohol at Pt electrodes. ACS. Catal. *10*, 6831–6842. https://doi.org/10.1021/acscatal.0c00818.

Wang, F., Li, C., Chen, H., Jiang, R., Sun, L.-D., Li, Q., Wang, J., Yu, J.C., and Yan, C.-H. (2013). Plasmonic harvesting of light energy for Suzuki coupling reactions. J. Am. Chem. Soc. *135*, 5588–5601. https://doi.org/10.1021/ja310501y.

Wang, F., Li, C., Sun, L.-D., Xu, C.-H., Wang, J., Yu, J.C., and Yan, C.-H. (2012). Porous single-crystalline palladium nanoparticles with high catalytic activities. Angew. Chem. Int. Ed. *51*, 4872–4876. https://doi.org/10.1002/anie.201107376.

Wang, J., Xu, C., Nilsson, A.M., Fernandes, D.L.A., Strömberg, M., Wang, J., and Niklasson, G.A. (2019). General method for determining light scattering and absorption of nanoparticle composites. Adv. Opt. Mater. *7*, 1801315. https://doi.org/10.1002/adom.201801315.

Weaver, J.H., and Benbow, R.L. (1975). Low-energy interband Absorption in Pd. Phys. Rev. B *12*, 3509–3510. https://doi.org/10.1103/PhysRevB.12.3509.

Xiao, Q., Sarina, S., Jaatinen, E., Jia, J., Arnold, D.P., Liu, H., and Zhu, H. (2014). Efficient photocatalytic Suzuki cross-coupling reactions on Au–Pd alloy nanoparticles under visible light irradiation. Green. Chem. *16*, 4272–4285. https://doi.org/10.1039/C4GC00588K.

Xin, H., Namgung, B., and Lee, L.P. (2018). Nanoplasmonic optical antennas for life sciences and medicine. Nat. Rev. Mater. *3*, 228–243. https://doi.org/10.1038/s41578-018-0033-8.

Yu, Y., Wijesekara, K.D., Xi, X., and Willets, K.A. (2019). Quantifying wavelength-dependent plasmonic hot carrier energy distributions at metal/semiconductor interfaces. ACS Nano *13*, 3629–3637. https://doi.org/10.1021/acsnano.9b00219.

Zhang, C., Jia, F., Li, Z., Huang, X., and Lu, G. (2020). Plasmon-generated hot holes for chemical reactions. Nano Res. *13*, 3183–3197. https://doi.org/10.1007/s12274-020-3031-2.

Zhang, S., Chang, C., Huang, Z., Ma, Y., Gao, W., Li, J., and Qu, Y. (2015). Visible-light-activated suzuki–miyaura coupling reactions of aryl chlorides over the multifunctional Pd/Au/porous nanorods of CeO_2 catalysts. ACS. Catal. *5*, 6481–6488. https://doi.org/10.1021/acscatal.5b01173.

Zhang, Y., He, S., Guo, W., Hu, Y., Huang, J., Mulcahy, J.R., and Wei, W.D. (2018). Surface-plasmon-driven hot electron photochemistry. Chem. Rev. *118*, 2927–2954. https://doi.org/10.1021/acs.chemrev.7b00430.

Zhang, Z.L., Zhang, C.Y., Zheng, H.R., and Xu, H.X. (2019). Plasmon-driven catalysis on molecules and nanomaterials. Acc. Chem. Res.

52, 2506–2515. https://doi.org/10.1021/acs.accounts.9b00224.

Zhao, J., Nguyen, S.C., Ye, R., Ye, B.H., Weller, H., Somorjai, G.A., Alivisatos, A.P., and Toste, F.D. (2017). A comparison of photocatalytic activities of gold nanoparticles following plasmonic and interband excitation and a strategy for harnessing interband hot carriers for solution phase photocatalysis. ACS Cent. Sci. *3*, 482–488. https://doi.org/10.1021/acscentsci.7b00122.

Zhou, L.A., Swearer, D.F., Zhang, C., Robatjazi, H., Zhao, H.Q., Henderson, L., Dong, L.L., Christopher, P., Carter, E.A., Nordlander, P., and Halas, N.J. (2018). Quantifying hot carrier and thermal contributions in plasmonic photocatalysis. Science *362*, 69–72. https://doi.org/10.1126/science.aat6967.

Zhu, H., Chen, X., Zheng, Z., Ke, X., Jaatinen, E., Zhao, J., Guo, C., Xie, T., and Wang, D. (2009). Mechanism of supported gold nanoparticles as photocatalysts under ultraviolet and visible light irradiation. Chem. Commun. 7524–7526. https://doi.org/10.1039/B917052A.

STAR★METHODS

KEY RESOURCES TABLE

REAGENT or RESOURCE	SOURCE	IDENTIFIER
Chemicals, peptides, and recombinant proteins		
Tetrahydrofuran	Fisher Chemical	Cat#T425-4
$PS_{(5000)}$-b-$PEO_{(2200)}$	Polymer Source Co.	Cat#P10131B-SEO
Hydrochloric acid, 37%	Thermo Scientific	Cat#AC450560050
Palladium(II) chloride	Alfa Aesar	Cat#43085
L-Ascorbic acid	Fisher Chemical	Cat#A61-25
Deuterated chloroform	Thermo Scientific	Cat#AC166251000
Dichloromethane	Thermo Scientific	Cat#AC610050040
Nitric acid	Fisher Chemical	Cat#T003090500
Precious Metals ICP Standard	Inorganic Ventures Co.	Cat#CCS-2-125ML
Bromobenzene	TCI America	Cat#B043925G
Phenylboronic acid	Thermo Scientific	Cat#AAA1425730
Cetyltrimethylammonium chloride	Thermo Scientific	Cat#AC411415000
Sodium hydroxide	Thermo Scientific	Cat#AC424335000
Biphenyl	TCI America	Cat#B046525G
Bromoanisole	Thermo Scientific	Cat#AAA118240E

RESOURCE AVAILABILITY

Lead contact

Further information and requests for resources should be directed to and will be fulfilled by the lead contact, Son C. Nguyen (son@ucmerced.edu).

Materials availability

All materials generated in this study are available in the article and supplemental information or from the lead contact without restriction upon reasonable request.

Data and code availability

- All data reported in this paper will be shared by the lead contact upon request.
- This study did not generate any datasets.
- Any additional information required to reanalyze the data reported in this paper is available from the lead contact upon request.

METHOD DETAILS

Synthesis of porous Pd nanoparticles

Mesoporous Pd nanoparticles were synthesized by following the method from the Yamauchi's group (Li et al., 2019). In a 7-mL glass vial, 200 μL THF (containing 8 mg $PS_{(5000)}$-b-$PEO_{(2200)}$, Polymer Source Co.), 160 μL HCl (2 M), 500 μL H_2PdCl_4 (76.8 mM), 1140 μL H_2O and 2000 μL ascorbic acid (0.1 M) were added and under stirring. The glass vial was then put in a water bath set at 50°C for 10 h reduction reaction to form a dark grey solution, followed by centrifuging at 14,100 g-force and washing with THF and water (3:1 volume ratio) for three times. Eventually, the final product was calcinated in a muffle furnace at 200°C for one hour to remove the solvent and most of the polymer.

Characterizations of nanoparticles, reaction solution and product

The mesoporous Pd nanoparticle photocatalyst was characterized by UV-vis spectroscopy (USB4000, Ocean Optics), DLS (Zetasizer Pro, Malvern Panalytical), SEM (Quanta 200, 5.0 kV, FEI), TEM (Talos

F200C G2, 200 kV, Thermo Fisher Scientific), FTIR spectroscopy (Nicolet iS50R, Thermo Fisher Scientific) and TGA (TA Q2000, argon flow at 100 mL/min, heating rate of 10°C/min, TA Instruments). The assignment of the weight lost was based on the TGA of similar polymers.(Deng et al., 2007; Iatridi et al., 2020). The biphenyl product was extracted from the reaction solution by dichloromethane, then the solvent was evaporated, and the product was dissolved in deuterated chloroform ($CDCl_3$) and quantified by ^{1}H-NMR (Varian-INOVA 400 MHz, Agilent Technologies) with mesitylene used as the internal standard. There was no signal of any other side products. The amount of leached Pd was determined by ICP-OES (Optima 5300 DV Inductively Coupled Plasma Optical Emission Spectrometer, PerkinElmer). The analyzed samples were prepared by collecting the supernatants after centrifuging the reaction solutions, followed by 800°C calcination to remove all the organics, digestion with aqua regia, dilution to a final 1-5% HNO_3 v/v concentration solution, and filtration with 0.2 μm filter. Standard solutions were prepared with trace-metal-free nitric acid from a commercial standard solution (ICP Precious Metal Std, Inorganic Ventures Co.) The surface oxidation state of porous Pd nanoparticles before and after reactions was detected by x-ray photoelectron spectrometer (Nexsa, Thermo Fisher Scientific) with monochromated, micro-focused, low power Al Kα X-ray source. The possible by-products generated from parallel processes were determined by GC-MS (7890A GC system and 5975C inert MSD, Agilent Technologies).

Typical photocatalyzed Suzuki–Miyaura reaction conditions

In a 1 × 1 cm quartz cuvette (R-3010-T, Spectrocell), 21 μL bromobenzene (0.2 mmol, 1 equiv.), 36 mg phenylboronic acid (1.5 equiv.), 495 μL CTAC (cetyltrimethylammonium chloride, 400 mM), 600 μL NaOH (sodium hydroxide, 1 M) and 884 μL porous Pd nanoparticles stock solution were added under stirring. The stock porous Pd nanoparticle solution was prepared by dispersing the dry particles in water to have the final ratio of 0.78% of [Pd_{atom}] to [bromobenzene] (0.0078 equiv.) in the reaction solution. Then, the cuvette was sealed by a screw cap with rubber septa, then stirred by a magnetic bar with 1000 rpm and purged with N_2 for 20 minutes to get rid of oxygen before being irradiated under different LEDs (Mounted type, Thorlabs). The photocatalyzed reactions were under constant stirring by a magnetic bar at 1000 rpm and controlled at room temperature by using cooling fans. The optical powers before and after the cuvette were recorded by power meters (PM100D console with S170C sensor, Thorlabs) for following calculation of absorbed photon flux. After a certain reaction time, the biphenyl product was extracted from the reaction solution by dichloromethane, then the solvent was evaporated at 50°C in a vacuum oven for 20 minutes, and the product was dissolved in $CDCl_3$ and quantified by ^{1}H-NMR with mesitylene used as the internal standard. The NMR spectra and product yield calculation were listed in supplemental information.

Quantum yield calculation

Using the same calculation in our previous work (Mao et al., 2019), the quantum yield is defined as the ratio of the number of biphenyl molecules produced per second ($\Delta N_{biphenyl}/\Delta t$) to number of photons absorbed per second (N_{abs}/s).

$$\text{Quantum Yield (\%)} = \frac{\#(\text{biphenyl produced}/s)}{\#(\text{photons absorbed}/s)} \times 100\,\% = \frac{\frac{\Delta N_{biphenyl}}{\Delta t}}{\frac{N_{abs}}{s}} \times 100\,\%$$

In which:

$$\Delta N_{biphenyl} = 0.2\ mmol \times \text{Product Yield} \times 6.022 \times 10^{23}\ mol^{-1}\ (*)$$

Δt: reaction time in second

$$\frac{N_{abs}}{s} = \frac{P_{absorbed}}{\frac{hc}{\lambda}}\ (**)$$

(*) The product yield of the photocatalyzed reaction was determined by ^{1}H-NMR spectroscopy and further corrected by subtracting the background product yield of the non-irradiated reaction within the same reaction time.

(**) (N_{abs}/s) were quantified by measuring the optical power at positions before and after the cuvette having the reaction solution during the photoreactions.

$$\text{Photon Flux}\left(\text{photons}\cdot s^{-1}\cdot cm^{-2}\right)=\frac{N_{abs}}{s\times A}=\frac{P_{\text{absorbed}}}{\frac{hc}{\lambda}\times\pi\left(\frac{\varphi}{2}\right)^2}$$

In which: φ is the beam size of the LED light that passes through the cuvette having the reaction solution. The beam size was 0.95 cm, which is smaller than the 1 cm width of the cuvette.

Surface area calculation

The specific Brunauer, Emmett and Teller (BET) surface area of the porous Pd nanoparticles was 57.1 m^2/g (Figure S4), which was around 7 times larger than that of the non-porous Pd nanoparticles with a silimar diameter (see calculations below). The pore volume of the porous Pd nanoparticles was 0.30 cm^3/g from the above measurement. The pore radius distribution acquired from Barrett-Joyner-Halenda (BJH) desorption showed an average pore radius of 2.8 nm, or a pore size of 5.6 nm. The difference of pore size from BJH (5.6 nm) and TEM (11.3 nm) data came from different perspectives of the two measurements and non-uniformity of pore structures.

Estimated surface area of 1 g spherical nonporous Pd nanoparticles with an average size of 60 nm:

Mass of one nanoparticle (m_1):

$$m_1=\rho\cdot V=\rho\cdot\left(\frac{4}{3}\pi r^3\right)$$

ρ : density of *Pd*, $12.023\times10^3\frac{kg}{m^3}$

V : volume of one nanoparticle

r : radius of one nanoparticle, $30\times10^{-9}\ m$

So, $m_1 = 1.360\times10^{-18}$ kg $= 1.360\times10^{-15}$ g.

Then, the number of nanoparticles in 1 g Pd (#):

$$\#=\frac{1\ g}{1.360\times10^{-15}\ \text{g}}=7.354\times10^{14}$$

Surface area for one nanoparticle (S_1):

$$S_1=4\pi r^2=1.131\times10^{-14}\ m^2$$

Thus, the estimated total surface area of the nonporous Pd nanoparticles (S_E) will be

$$S_E=\#\cdot S_1=8.32\ m^2/g$$

Light scattering measurement

Drop-cast sample. A thin film of the sample was prepared by spin coating (1000 rpm, 45 sec, KW-4A Spin Coater, Chemat Technologies.) on a transparent circular quartz substrate with a diameter of one inch. An integrating sphere (Barium sulfate coated, Newport Corp.) was used for measuring scattering cross sections by collecting diffusely transmitted and reflected light. A tunable laser system (430 nm–700 nm, 400 mW, SuperK Extreme Supercontinuum, NKT photonics) was used as a light source. The scattered light was collected at the 90° port of the integrating sphere for both diffused transmission and diffused reflection by a spectrometer (Acton SP2300, Princeton Instruments). The schematic of the experimental setup is shown in Scheme S1.

Colloidal sample. The purpose of this experiment is to ensure that the scattered light from the photocatalyzed reaction is negligible as compared to the absorbed light during the photoreaction. Briefly, the Xe lamp (300 W Research Arc Lamp Source, Newport Corp.) was set at 60 W, a 1.5 inch liquid water filter was used to remove the unwanted IR light, and the UV-vis light was collimated and sent the colloidal sample. Two neutral density filters (OD ~1.1 for each) were inserted into the transmitted path to lower the light intensity at the detector. An optical fiber (300 μm Premium, Ocean Optics) coupled to a collimating lens (74-UV, Ocean Optics) was set to detect scattered and transmitted light from the sample (Scheme S2). The other end of the fiber was connected to an UV-vis spectrometer (USB4000, Ocean Optics). The colloidal sample was prepared by

dispersing 0.4 mg of mesoporous Pd nanoparticle powder in 2 mL of H_2O and transferred to a 1 × 1cm quartz cuvette for the measurement. A similar setup for scattering and extinction measurement can be found in literature (Liu et al., 2015; Wang et al., 2019). The scheme of experimental setup is shown in Scheme S2.

Extinction (E), scattering (S) and absorption (A) calculation. As seen from the above scheme, the transmitted light intensity after the light source passes through the colloidal nanoparticles should be corrected by the scattering background of water and the used cuvette. This transmitted light intensity at each wavelength, I_T (Sample), is defined as:

$$I_T(\text{Sample}) = \frac{I_T(H_2O) - I_T(\text{Sample in } H_2O)}{10^{-2OD}}$$

where:

I_T (H_2O): the measured transmitted intensity of pure water.

I_T (Sample in H_2O): the measured transmitted intensity of colloidal nanoparticles in water.

Note that a factor of 10^{-2OD} was used to account for the attenuation of the transmitted beam by the two neutral density filters.

Besides, the intensity of the incident light before the cuvette, (I_0), is calculated based on the transmitted light intensity of the pure water sample:

$$I_0 = \frac{I_T(H_2O)}{10^{-2OD}}$$

Similarly, the scattering intensity at a scattering angle of 90°, $I_{s,\,90}$ (Sample), is defined as:

$$I_{s,90}(\text{Sample}) = I_{s,90}(\text{Sample in } H_2O) - I_{S,90}(H_2O)$$

where:$I_{S,90}(H_2O)$: the measured scattering intensity of pure water.$I_{s,90}$ (Sample in H_2O): the measured scattering intensity of colloidal nanoparticles in water.

To account for the total scattered photons at all scattering angles, a geometric scaling factor of 7.84 was used. This factor was calculated based on the ratio of the collecting area of the used collimating lens to the estimated surface area of a sphere having a radius from the center of the cuvette to the collimating lens. This estimation is reasonable since our mesoporous particles follow Rayleigh scattering (see Figure S6), hence the scattering intensity is even at any angles (He et al., 2009). Thus, the total scattering intensity is determined as: $I_s(\text{Sample}) = 7.84 \times I_{s,90}(\text{Sample})$).

From the above experimental data, the scattering-over-extinction ratio was calculated based on a similar method reported by Ren's group (Liu et al., 2015). The extinction intensity (I_E) of the sample is the sum of the absorption (I_A) and scattering intensities (I_S):

$$I_E = I_A + I_S$$

The incident light intensity is the sum of the extinction and transmitted light intensities:

$$I_0 = I_E + I_T = I_A + I_S + I_T$$

Then, the extinction (E), scattering (S) and absorption (A) are calculated as:

$$E = -\log_{10}\frac{I_T(\text{Sample})}{I_0} = -\log_{10}\frac{I_T(H_2O) - I_T(\text{Sample in } H_2O)}{I_0 \cdot (10^{-2OD})}$$

$$A = -\log_{10}\frac{I_T(\text{Sample}) + I_s(\text{Sample})}{I_0}$$

$$S = E - A = -\log_{10}\frac{I_T(\text{Sample})}{I_T(\text{Sample}) + I_s(\text{Sample})}$$

Effect of local heating on the observed photocatalysis

The photothermal effect on the observed photocatalysis has been alerted recently in some previous experiments.(Dubi et al., 2020; Jain, 2019). Note that our "continuous-wave irradiation and stirring" condition is very different from other experimental conditions in which pulse laser was used and heat dissipation was poor. Local heating, the temperature rise in the vicinity of individual nanoparticles in our experiment, should be neglectable after considering the three timescales of the three below processes after a nanoparticle absorbs a photon.

The first timescale is the relaxation time of the hot carriers, which eventually converts the energy of an absorbed photon into heat in the nanoparticle. The longest observed time for this relaxation is about few picoseconds for gold nanoparticles (Minutella et al., 2017). The hot carriers are well thermalized within these few picoseconds due to the ultrafast electron-electron and electron-phonon couplings (Link and El-Sayed, 2000), and the nanoparticles should have an even temperature distribution within this timescale. Thus, it is reasonable to estimate the temperate rise of the particle based on the energy of a single photon absorbed, the specific heat of the metal and the mass of a single nanoparticle. This temperature rise was estimated well below 1°C in a previous study (Zhao et al., 2017). In our experiment, the temperature rise for each mesoporous Pd particle are about 0.00131 or 0.00113°C for a 405 or 470 nm photon absorbed, respectively (see the calculation in Table S9).

The second timescale is the time for the heat transfers from the nanoparticle to the surrounding environment. This timescale for colloidal gold nanoparticles in water is about two to three nanoseconds (Nguyen et al., 2016). Although this timescale was measured for gold nanoparticles, it is reasonable to assume that the heat dissipation from our mesoporous Pd nanoparticles to water is completed within 3 nanoseconds.

The third timescale is the period between the two photons can be absorbed by the same nanoparticle. Since we know the number of photons absorbed in the colloidal solution and the amount of nanoparticles in the beam path, we can estimate the average number of photons absorbed by individual nanoparticle under each second of irradiation. The table shows that the third timescale is roughly 293 nanoseconds under a typical experimental condition in our study. In an extreme case, a 470 nm LED with incident power of 502 mW causes an absorption of 282 mW in the reaction solution, the corresponding third timescale is about 73 nanoseconds. It is obvious that some nanoparticles may diffuse in and out of the LED beam area during this third timescale, but we can ignore this effect since the beam size is quite big. Besides, on the timescale of hundreds of nanoseconds, the percentage of nanoparticles diffusing in and out of the LED beam is quite small. Note that the absorption is not uniform across the entire area of the LED beam. However, the absorbance of the reaction solution is quite low, about 0.42 OD for all wavelengths, thus there is no huge change in the absorption profile. Overall, the approximated third timescales are very large as compared to the above second timescale, thus the nanoparticle dissipated all the heat long before the time it absorbs another photon (Khurgin, 2020). Under our stirring condition, the accumulated heat in the beam path is effectively transferred to the entire cuvette (Un and Sivan, 2021). With a cooling fan, the reaction solution in the cuvette only has a temperate rise within 1-2°C.

ICP-OES analysis for Pd in reaction supernatant

See calibration curve in Figure S10 and results in Table S10. An amount of 1 mL of the supernatant (total reaction volume = 2 mL) was used in the ICP-OES analysis. The sample digestion and preparation processes were shown in Characterizations section. The final volume of analyzed samples was 10 mL. The amount of Pd used in each reaction was 0.00156 mmol (0.1660 mg). Considering the lowest concentration of the standard curve (0.1 ppm) which approaches the detection limit of the instrument, it is reasonable to use 0.1 ppm as the upper-limit of the leached Pd amount in the analyzed samples. Thus, the utmost amount of leached Pd in the supernatant was 0.2 ppm, which is about 1.2% of the total Pd in the nanoparticle photocatalyst.

XPS analysis of porous Pd nanoparticles

In order to compare the oxidation state of Pd on the surfaces of the photocatalysts before and after Suzuki reaction, some contrast samples were designed as listed in Table S11. The assignment of respective peaks

was based on the handbook of XPS (Chastain and King Jr, 1992) and chemicals used for the reaction. The XPS spectra for four contrast samples are shown in Figure S12.

The presence of Pd, O, and C elements was observed across all samples in the survey spectrum Figure S12. For the as-prepared porous Pd nanoparticles, there was no bromine or nitrogen occurred in the sample, indicating a relatively clean surface of the initial catalysts. Also, the narrow and distinct peak in Pd 3d at 335.0 eV and 340.2 eV matched with the Pd $3d_{5/2}$ and Pd $3d_{3/2}$, which meant the oxidation state of Pd in the as-prepared sample was mostly zero on the surface. The result was consistent with the previous report from Yamauchi's group (Iqbal et al., 2017). The occurrence of carbonates in the C 1s and O 1s spectra was due to the atmospheric carboxylic acids absorbed on the surface (Balajka et al., 2018). The peak at 532.8 eV in O 1s was assigned to the oxidation layer of the silicon wafer used as a substrate for XPS measurement or adventitious contamination from the atmosphere.

After one-hour equilibrium with reaction mixture, the Pd 3d peaks became broader and demonstrated a tiny shoulder peak at higher binding energy but the positions did not shift from the Pd(0) state, probably resulting from the adsorption and activation of bromobenzene on porous Pd surface (Gniewek et al., 2005). Also, the occurrence of hydroxides in the O 1s spectrum was due to the phenylboronic acid and sodium hydroxides used for the Suzuki reaction.

After 6-hour dark reaction, the Pd 3d peaks were still broad compared to the as-prepared sample but still within the range of the Pd(0) state. The noisy background was possibly from multiple kinds of organic absorbates remaining on the surface. Besides, the occurrence of bromine was distinct in Br 3d spectrum compared to the as-prepared sample and Porous Pd NPs-d-1 h, which could be coming from the residual bromide ion absorbed strongly on the Pd surface after certain amounts of Suzuki reaction catalytic cycles (Fu et al., 2014). Also, the O 1s peak position was located between the substrate and hydroxides, indicating the proceeding of the reaction.

In terms of the photocatalytic reaction under 405 nm LED for 6 hours, the narrow Pd 3d peaks were almost identical with that in the as-prepared porous Pd nanoparticles, revealing a similar oxidation state of Pd(0) before and after the photocatalytic reaction. This identity was also applied to the C 1s and O 1s peaks, revealing a relatively clean surface of porous Pd nanoparticles after the photocatalytic reaction. It may be due to the surface self-cleaning effect by holes generated during photocatalysis, similar to the widely-studied case of titanium oxide photocatalysts (Fujishima et al., 2008). Moreover, the leftover bromide ion from the reaction and ammonium salt or organic matrix from the solubilizer CTAC were observed in Br 3d and N 1s spectra.

In general, there were no distinct shifts of Pd 3d peaks across the four samples and the analysis of all potential elements on porous Pd nanoparticles' surface illustrated that the oxidation state of Pd did not change before and after the reaction, either in the dark or photocatalytic conditions.

Control experiments to confirm that hetero-coupling is the only product

Under our standard reaction between bromobenzene and phenylboronic acid, the hetero- and homo-coupling product, biphenyl, is indistinguishable. As shown in control experiments reported in Table S7, there was no biphenyl product when either bromobenzene or phenylboronic acid was used. Still, other control reactions with an expected unsymmetric product are necessary to confirm the presumed hetero-coupling process under our reaction conditions. The reaction between 4-bromoanisole and phenylboronic acids was conducted to validate the hetero-coupling as shown below:

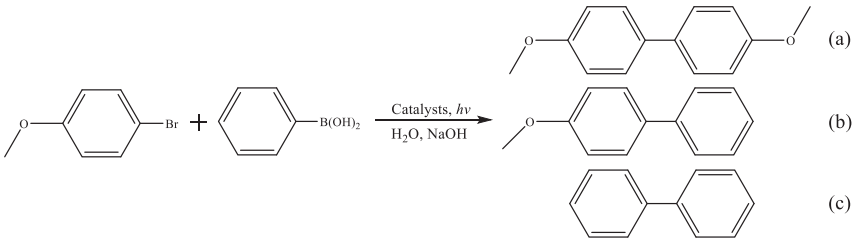

The homo-coupling product would be 4,4′-dimethoxy-1,1′-biphenyl (a) or biphenyl (c), while the hetero-coupling product would be 4-methoxy-1,1′-biphenyl (b). All reaction conditions were conducted as the same as the typical condition except for the replacement of bromobenzene by 4-bromoanisole. See results in Table S12 and NMR spectra in Data S1.

Exclusion of some other parallel processes besides the Suzuki-Miyaura reaction

Considering some other possible processes that could happen in parallel to the Suzuki-Miyaura reaction. Under photocatalytic reaction conditions, there may be some parallel processes that may be concurrent to the proposed photocatalyzed reaction. For example, the debromination (a), substitution by a hydroxyl group of the reactant (b), or deborylation (c) may occur as shown below:

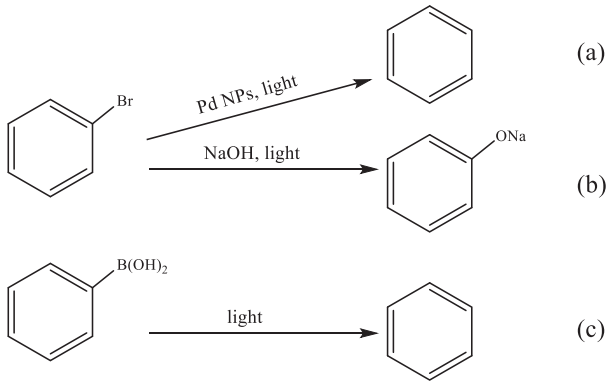

Experimental design to exclude the above possible processes. The reagents that were involved in above processes were abbreviated as listed for convenience. Ph-Br for bromobenzene, Ph for benzene, Ph-$B(OH)_2$ for phenylboronic acid, Ph-Ph for biphenyl, Ph-ONa for sodium phenolate, Ph-OH for Phenol, and DCM for dichloromethane. GC-MS for gas chromatography-mass spectrometry.

In general, our strategy here was to extract any side products from crude reaction mixture by DCM (both from organic or aqueous phase) and directly send the solution for GC-MS analysis. Two standard sample vials, noted as A and B here, were prepared: (i) Vial A for detecting processes a and c; (ii) Vial B for process b. Vial A contained Ph-Br, Ph, and Ph-Ph (0.2 mmol for each) in 1 mL DCM. Vial B contained Ph-Br, Ph-OH, and Ph-Ph (0.2 mmol for each) in 1 mL DCM.

Secondly, the procedure of reaction mixture post-processing was optimized a little bit to test above processes. After photocatalytic reaction (in this note, 405 nm LED chosen as an example, referred to the typical reaction condition in entry 2 of Table S4), the crude reaction mixture was extracted by 1 mL DCM to retrieve the organic compounds from the aqueous solution, which was labeled as 405-O. And the leftover aqueous solution from the previous step was extracted by 1 mL DCM after adding 600 μL hydrochloric acid (HCl, 1M, to neutralize the basic solution and convert Ph-ONa to Ph-OH), which was labeled as 405-H. Those samples were directly sent for the GC-MS analysis. See GC-MS spectra in Data S2.

Analysis results. In the GC-MS spectra of vials A and B, the retention time of Ph, Ph-Br, Ph-OH, and Ph-Ph were well separated in the total ion chromatogram and the MS spectra of those chemicals were well aligned to their mass fragments. Thus, any potential by-products could be detected and distinguished from the reactants in the photocatalytic reaction.

As for the sample 405-O (directly extracted from reaction mixture), the GC spectrum demonstrated a tiny amount of Ph generated compared to the Ph-Ph formed, suggesting that the processes (a) and (c) in part (1) may occur during photocatalytic reaction. However, considering its relatively low amount, those processes should not be considered as major side-reactions to the Suzuki reaction process. Similarly, for the sample 405-H, the process (b) may happen but not contribute a lot to the Suzuki reaction. One thing to mention here, the product occurred in the sample 405-H due to the solubilizer CTAC used in the reaction which would bring a certain amount of organic compounds into the aqueous phase (which was shown to be

less than 10% amount of the total organics in the aqueous solution in a separate experiment, not shown here).

Overall, the deborylation/debromination or, probably, substitution by hydroxyl group of the reactants may occur during the photocatalytic reactions by porous Pd nanoparticles but proved to be negligible compared to the formation of desired biphenyl product.

NMR spectra of standard compounds and typical reaction solutions, and product yield calculation

NMR spectra of standard samples were shown in Figure S13. The targeted product biphenyl yield was calculated from integration of the peak area at δ 7.58–7.52 (m, 2H) with the known amount of internal standard mesitylene at δ 6.87 (s, 3H). NMR spectra of typical Suzuki reaction solutions are shown in Data S3.